Journal of Materials Chemistry C

ROYAL SOCIETY OF CHEMISTRY

PAPER

View Article Online
View Journal | View Issue

Cite this: J. Mater. Chem. C, 2020, 8, 1656

Liquid metal-supported synthesis of cupric oxide†

Hongzhe Li,[a] Roozbeh Abbasi,[a] Yifang Wang,[a] Francois M. Allioux,[a] Pramod Koshy,[b] Shuhada A. Idrus-Saidi,[a] Md Arifur Rahim,[a] Jiong Yang,[a] Maedehsadat Mousavi,[a] Jianbo Tang,[a] Mohammad B. Ghasemian,[a] Rouhollah Jalili,[a] Kourosh Kalantar-Zadeh *[a] and Mohannad Mayyas*[a]

Received 17th December 2019,
Accepted 20th December 2019

DOI: 10.1039/c9tc06883j

rsc.li/materials-c

Liquid metal interfaces with their unique chemistry can provide an extraordinary tool to synthesise materials with controlled characteristics at room temperature. Here, the templated synthesis of cupric oxide (CuO) onto a gallium based liquid metal (galinstan) surface is explored. The interaction between galinstan and copper sulphate solution yields initial interfacial CuO sheets and then secondary dendritic nanostructures are grown from the sheets. It is shown that the pH of the aqueous environment plays a critical role in tuning the synthesis of substoichiometric Cu_xO to CuO. For enhancing the interfacial area and establishing heterojunctions, the liquid metal is processed into a suspension of micro and nano droplets by sonication and the example of using the synthesised nano structures for enhanced photocatalysis is demonstrated for the catalysis of a model dye. This study presents a facile approach for synthesising highly functional systems based on liquid metals, and it can be extended to explore other metal oxide–liquid metal composites.

Introduction

Liquid metals (LMs) have received attention due to their distinct interfacial chemistry that remains largely unexplored. The atomically ultra-smooth interfaces of LMs establish a promising platform for templating materials with unique morphologies.[1–3] The two most well-known examples of room temperature gallium based LM alloys are EGaIn (the combination of gallium and indium as a binary alloy) and galinstan (the combination of gallium, indium and tin as a ternary alloy). The melting points of these LM alloys are below room temperature, EGaIn at 15.7 °C and galinstan even lower.[4–14]

A few recent studies have shown that the LM-solution interfaces can be utilised to fabricate smooth and ultrathin films.[15] When exposed to an oxic environment, a self-limiting oxide skin forms at the interface of LMs with the environment in their vicinity, which can be easily exfoliated due to the minimal interfacial forces between the forming layer and the non-polar LM.[16] Similarly, other forms of laminar compounds can be accessed by manipulating the chemistry at the interface.[17]

Due to their fluidity under ambient conditions, LMs can be broken down into micro and nano droplets by applying shear force, allowing the interfacial area to be tuned to the desired size.[1,18,19] Attractive features of these broken down LMs have shown peculiar promise for diverse applications such as drug delivery,[20] bioimaging,[13] flexible electronics,[21–25] and advanced material synthesis.[15]

In addition to the aforementioned-applications for LMs, catalytic systems based on LMs have also started to present great prospects.[15,26–29] One of the intriguing aspects of using LMs as catalysts is that their catalytic activity can be tailored either by alloying with specific elements and/or tuning them with interfacially added materials. The surface composition and functionalisation of LMs have offered the possibility of significantly enhancing catalyst activity and selectivity toward specific reactions.[1,26,30] The ability of breaking down LMs into micro and nano liquid droplets is another distinct attribute, which is essential to enhancing the surface area and hence the catalytic performance of LMs.[31] By controlling the interfacial chemistry, it is possible to fabricate surface-confined nanostructures of various metal oxide semiconductors onto the LM droplets.[2,15,32] The resulting composites of LMs and metal oxide semiconductors generally feature superior photocatalytic performance when compared to that of their individual entities. Such an enhancement in performance is generally attributed to the inhibition of free carrier recombination in the semiconductor–LM junction.[15,33,34] One of the catalytic semiconductors with well-known semiconductor and optical performance is cupric oxide that can be synergically incorporated onto the surface of liquid metals.

[a] School of Chemical Engineering, University of New South Wales (UNSW), Sydney, NSW 2052, Australia. E-mail: k.kalantar-zadeh@unsw.edu.au, m.mayyas@unsw.edu.au
[b] School of Materials Science and Engineering, University of New South Wales (UNSW), Sydney, NSW 2052, Australia

† Electronic supplementary information (ESI) available. See DOI: 10.1039/c9tc06883j

Cupric oxide (CuO) is commonly a p-type semiconductor with a band gap of ~1.2 eV. It is widely used in the fields of gas sensing,[35] catalysis,[36] photoconversion[37] and energy storage.[38] In addition, the use of CuO for water treatment (*i.e.*, dye photodegradation) has received significant attention. For example, CuO with different morphologies including nanofilms,[39] nanowires,[40,41] nanoparticles[33,42–45] and nanoflakes[46] has been synthesised and tested for photodegradation. The photodegradation performance of CuO has been shown to enhance significantly when combined with other materials, *e.g.*, with ZnO,[47] TiO_2[48] and reduced graphene oxide.[49] Inspired by these examples, we hypothesised that the synergism between the LM and CuO may lead to the formation of a composite system with tuneable composition and interfacial properties suited for high performance photocatalysis.

The synthesis of CuO is a pH dependent process that has to be controlled to avoid the formation of other secondary phases such as Cu and Cu_2O,[36] which are metallic and have a wider band gap, respectively, rendering them less efficient for photocatalysis. With other synthesis techniques such as chemical precipitation[50] and hydrothermal synthesis,[51] producing a single phase CuO requires strict control and elevated temperature, which are, in most cases, challenging. In the current study, we report a new controllable approach to synthesise CuO at room temperature. We demonstrate that the formation of CuO with distinct phase separation can be achieved. Furthermore, this method has been extended to fabricate a composite of CuO–LM. As a representative example, we show that the resulting CuO–LM composite offers an enhanced photocatalytic activity toward methylene blue photodegradation.

Material and methods

Materials

Gallium (round shots, 99.9%), indium, (beads, 99.9%) and tin (popcorn cakes, 99.9%) were purchased from Rotometals, USA. Copper(II) sulfate pentahydrate ($CuSO_4 \cdot 5H_2O$, 99.5%) was obtained from Chem-Supply Pty Ltd. Ammonium hydroxide solution (NH_4OH, 25%) was purchased from Acros Organics. Methylene blue (molecular weight of 319.85) was purchased from Sigma Aldrich. Sodium hydroxide (NaOH) pellets were obtained from Chem-Supply Pty Ltd.

Experimental

Gallium (68.5 wt%), indium (21.5 wt%) and tin (10 wt%) were added into a glass vial and heated at 250 °C on a hotplate for 15 min. When the mixture was melted, it was stirred to ensure homogeneity. The mixture was then left to cool down at room temperature.

Different concentrations of NH_4OH were tested to explore the optimum concentration of NH_4OH for synthesising the oxides of copper. In this set of experiments, 50 μL of 1.0 M NaOH solution was added onto a galinstan droplet (120 μL) in a glass Petri-dish.

This step was essential to remove the gallium oxide skin present at the interface. The NaOH solution was left on galinstan for 2.0 min before it was removed using a Pasteur pipette. As schematically presented in Fig. 1A, 4.0 mL of a solution containing various concentrations of NH_4OH and 0.50 mL of 0.01 M $CuSO_4$ solution was then added sequentially over the galinstan droplet. In subsequent experiments for pH optimisation, the concentration of NH_4OH was chosen as 0.25 M. Stock solutions with pH of 9.5, 10, 10.5 and 11 were prepared by adding 50, 30, 14 and 4 mL of 0.010 M $CuSO_4$, respectively, to 8.0 mL of 0.25 M NH_4OH. To develop Cu_xO on galinstan, approximately 4.5 mL of stock solution was added over galinstan (120 μL). The solution was left to react with the surface of galinstan for a specified period of time. For further analysis, the product was exfoliated from the LM surface by touch printing (Fig. 1B) on Si–SiO_2 wafer for Raman and X-ray photoelectron spectroscopy, and Si wafer for electron microscopy.

As schematically presented in Fig. 1C, to prepare LM micro and nano droplets covered with Cu_xO, 10 μL of galinstan was added into 20 mL of deionised (DI) water (18.2 MΩ cm at 25 °C), then the mixture was bath sonicated for 60 min until the large LM droplet was broken down to form a stable grey suspension. The micronised LM droplets were then separated by using a centrifuge (Thermoline scientific, Australia) at ~3500 RCF for 5.0 min. The precipitate, a grey paste that consists of broken down LM droplets, was separated from the supernatant by decantation and was then added into 4.5 mL of stock solutions separately at the pH of 9.5, 10, 10.5 and 11 to prepare 4 different samples. After 45 min of reaction time, the mixture was centrifuged as mentioned earlier. The precipitate was resuspended in DI water and then centrifuged at ~3500 RCF for 5.0 min. This centrifuge step was repeated to ensure that the product is clean from any $CuSO_4$ ions. The procedure was repeated several times for the sample obtained at pH = 10.5 to obtain enough material for photodegradation tests.

Characterisation

A Renishaw inVia Raman microspectrometer (Gloucestershire, UK) with 532 nm laser was utilised in this work. Specimens were prepared by drop-casting samples on a SiO_2–Si wafer and drying at room temperature. A Philips CM200 field-emission high-resolution transmission electron microscope (HRTEM) equipped with a GATAN ORIUS camera for direct depiction of digital images was utilised to investigate the structure of the product. The Cu_xO product was directly collected from the reaction system and drop-casted on a lacey carbon grid 20 (Ted Pella ultrathin carbon film on a lacey carbon support, 400 mesh, Cu). The gird was placed into the HRTEM instrument with a single-tilt holder. Scanning electron microscopy (SEM) images were taken using a JSM-IT500HR InTouchScope SEM instrument. In order to prepare SEM specimens, samples were drop-casted on silicon (100) wafers that were then attached on a carbon tape and loaded into the SEM instrument. The parameters were selected as follows: 5.0 kV accelerating voltage, 50 standard probe current and 10 mm working distance.

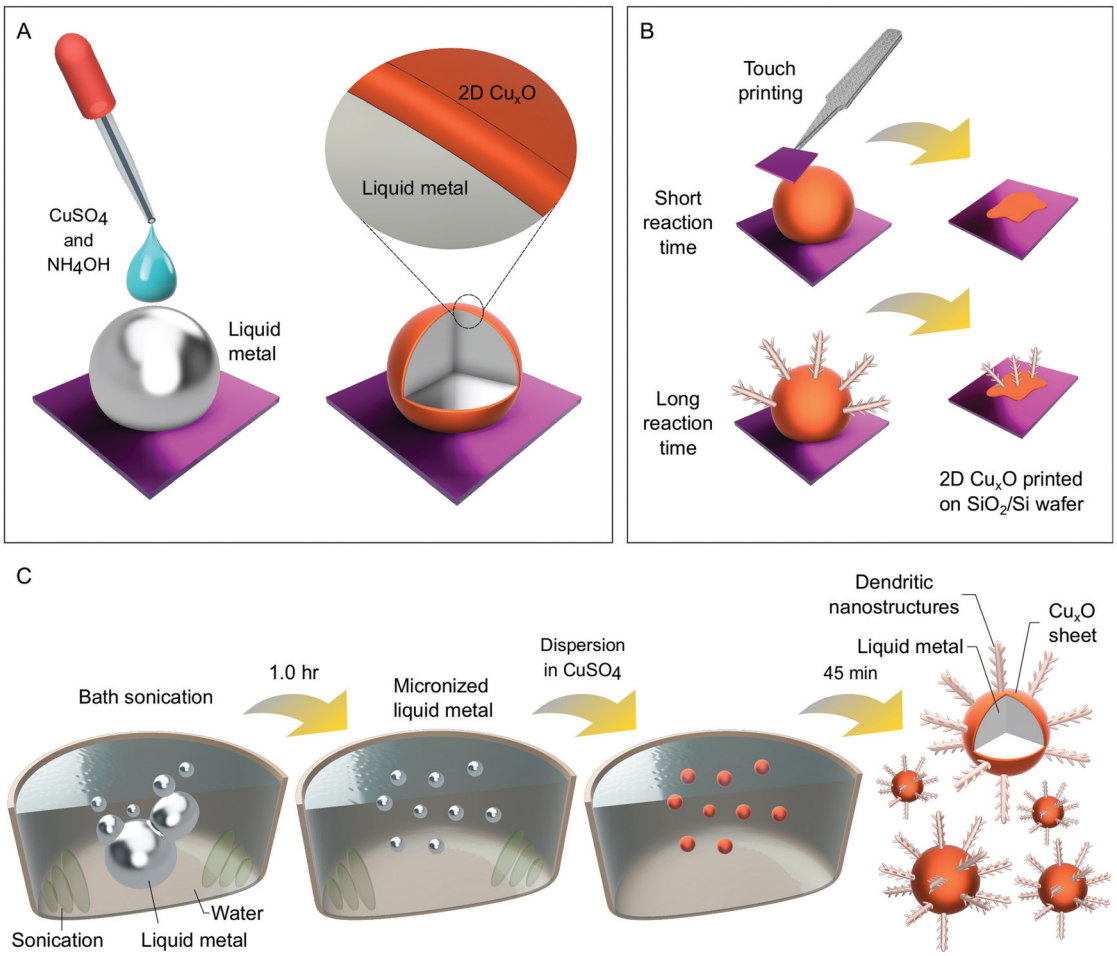

Fig. 1 Schematic representation of the synthesis of Cu_xO on the LM. (A) Cu_xO formation on the surface of large LM droplets. (B) Touch printing and exfoliation of the Cu_xO sheets onto wafers. (C) Sono-micronisation of LM into micro and nano droplets in water, and the formation of Cu_xO–LM micro-nano composites.

X-ray photoelectron spectrometry (XPS) patterns were collected using a Thermo Scientific ESCALAB250i high-resolution XPS (UK) instrument using a monochromatic Al Kalpha soft X-ray source (1486.68 eV). The scanning parameters were selected as follows: 2×10^{-9} mbar background vacuum, 120 W power (13.8 kV × 8.7 mA), 90° photoelectron take-off angle, and 500 μm spot size. For UV-vis spectroscopy, a Cary 5000 UV-vis NIR Spectrophotometer (Agilent Technologies, United States) in solid-phase (model number DRA-2500) was utilised to investigate the direct band gap of samples. For specimen preparation, samples were drop-casted on transparent quartz wafers (2.0 cm × 2.0 cm), and were then dried under ambient conditions. The scanning parameters were selected as follows: 200–2000 nm scanning range, 2.0 nm spectral bandwidth and double beam mode. Powder X-ray diffraction was undertaken using a Panalytical X'Pert – PRO PW3050/60 diffractometer (480 mm diameter) with a PW3064 sample spinner and an X'Celerator (2.122° active length) 1D-detector. An incident beam Soller slit of 0.04 rad, 1° fixed anti scatter slit, an incident beam mask of 10 mm and a programmable automated divergence slit giving a constant illuminated length of 10 mm were used. Data collection was performed from 5 to 100° 2θ at a 0.026° step with a scan speed of 118.3200 s per step. Phase analysis, Rietveld refinement and quantification were performed with the HighScore Plus 9.5 software package.

Photodegradation

The photocatalytic performance of the LM–CuO composite synthesised at pH = 10.5 was assessed in the photodegradation of methylene blue. The characteristic absorption peak for methylene blue is at 665 nm, which was selected for recording degradation performance at different times. The degradation performance of methylene blue with adding the catalyst was studied under the simulated intensity of one sunlight (Abet Technologies' model 11 002 SunLite Solar Simulators, ASTM Class A). For the photodegradation tests, a concentration of 0.20 mg of the catalyst per 1.0 mL of methylene blue solution was utilised. The resulting mixture was stirred at a constant rate of 500 rpm while being irradiated under the solar simulator. The absorbances of the photodegraded methylene blue were measured by UV-vis spectroscopy and were recorded at 5, 10, 30, 60, 90, and 120 min, respectively. The tests under

identical conditions were repeated two more times with the recycled catalyst from the previous tests.

Results and discussion

As explained in the Methods section, first, different concentrations of NH_4OH were explored for synthesising the oxides of copper onto a bulk of liquid metal. Raman spectroscopy was used for assessing the product composition. In the first stage of synthesis, the optimum concentration of NH_4OH that could produce single phase CuO was assessed. It was initially observed that varying the NH_4OH concentration leads to a minimal change in pH. To adjust the pH of the reaction system, the amount of $CuSO_4$ solution was controlled to reach the required pH as mentioned earlier in the Experimental section.

Cupric and cuprous oxides exhibit different zone-centre optical phonon modes and therefore, distinct Raman shifts for these two copper phases can be observed.[52–54] Cuprous oxide typically shows three major Raman peaks at approximately 153, 219, and 630 cm^{-1}, which respectively correspond to the first order Raman allowed mode (Γ_{25}), second order Raman allowed mode ($2\Gamma_{12-}$) and Infrared allowed mode ($B_g^{(2)}$).[52] Cupric oxide, on the other hand, has nine zone-centre optical phonon modes, and only three of them can be detected by Raman spectroscopy. These three modes are named as A_g, $B_g^{(1)}$ and $B_g^{(2)}$, corresponding to the Raman peaks at approximately 282, 330 and 625 cm^{-1}, respectively.[53] Considering the different signatures from the obtained Raman spectra, variations in composition are observed when the NH_4OH concentration is changed (Fig. 2A). Below 0.20 M, Cu_2O dominates while in the range between 0.25 and 0.40 M, the Raman modes of CuO become evident. A transition toward a mixture of both phases is achieved when the NH_4OH concentration is greater than 0.40 M. Since CuO was the product of interest, we fixed the NH_4OH concentration to be 0.25 M, the concentration at which CuO was dominant. Further control of solution chemistry was necessary to obtain the CuO in its purest form. From there, the effect of pH on the composition of the templated material was investigated. The pH was controlled by varying the amount of $CuSO_4$. Both pH and reaction time were studied (Fig. 2B–D); although the reaction time seems to have no significant influence on the product composition, the pH resulted in distinct transitions between CuO and Cu_2O. Raman modes of CuO (A_g, $B_g^{(1)}$ and $B_g^{(2)}$) are observed at pH $\geq$ 10.5.

To further confirm the composition of copper oxide products at different pH, XPS spectra were obtained. Fig. 3A shows the

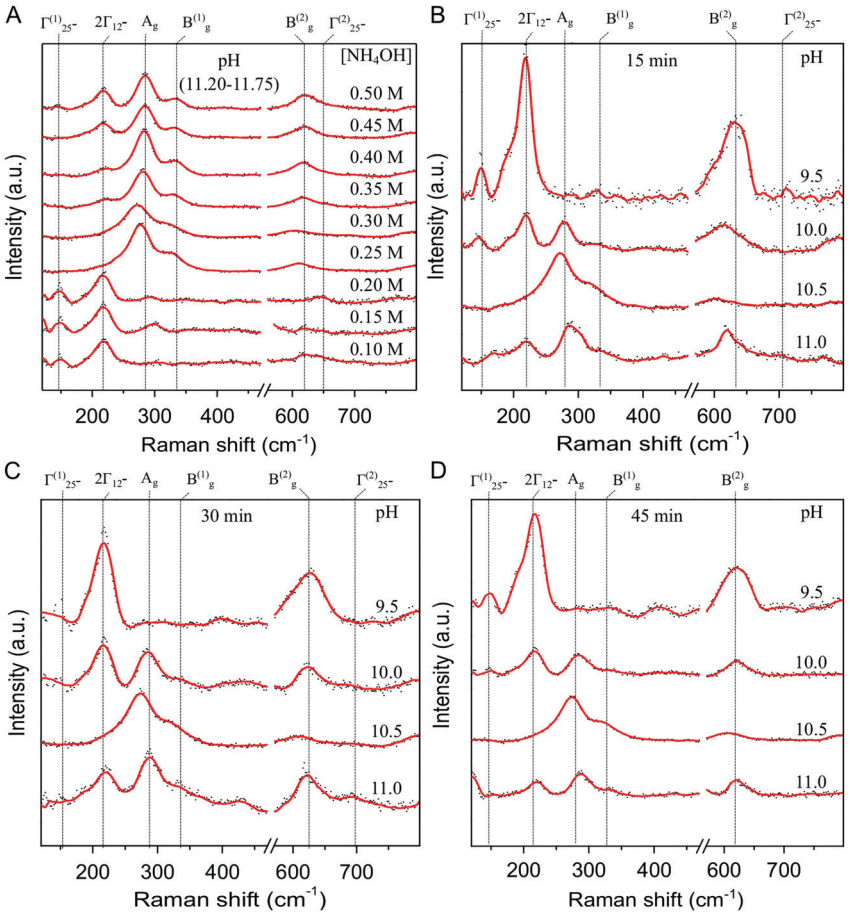

Fig. 2 Raman spectra of Cu_xO products. (A) Cu_xO samples produced at different NH_4OH concentrations. (B–D) Cu_xO samples produced at different pH at 15, 30 and 45 min, respectively.

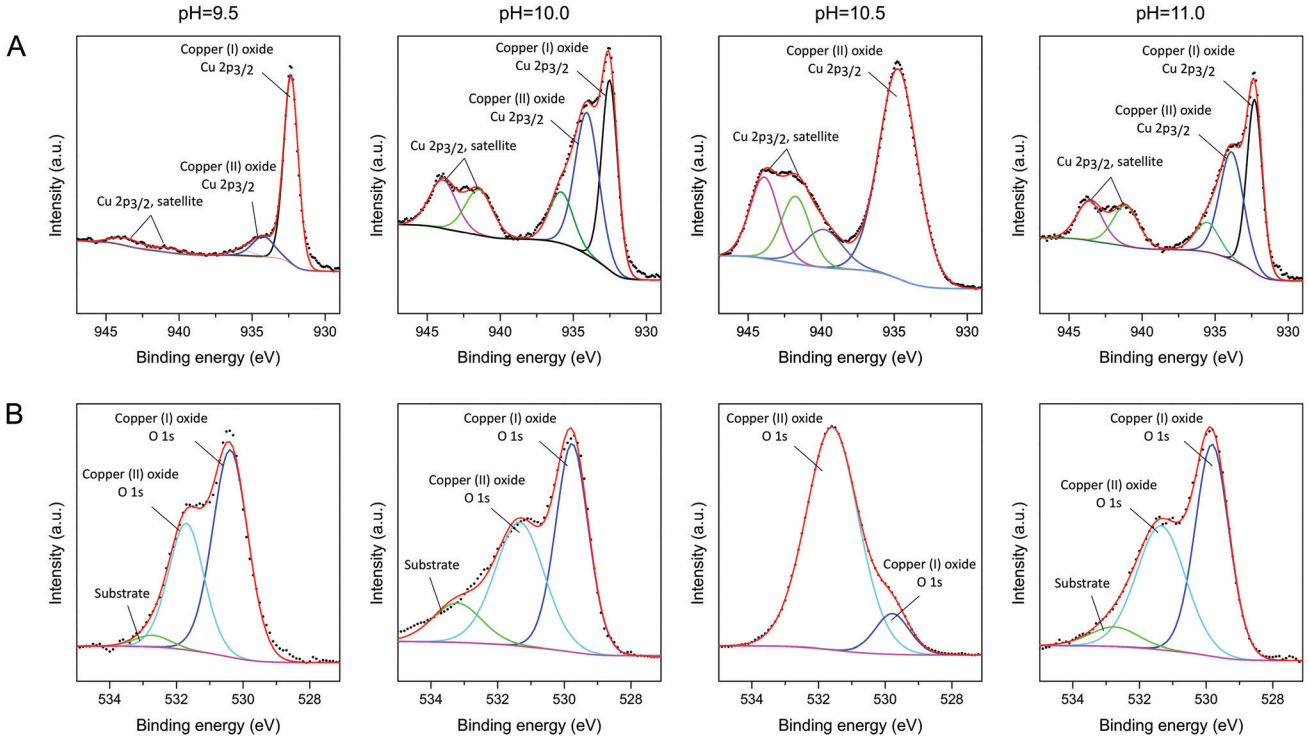

Fig. 3 High-resolution XPS patterns of the Cu_xO samples produced at different pH. (A) Deconvoluted XPS patterns of the Cu $2p_{3/2}$ region and (B) O 1s region.

Cu $2p_{3/2}$ spectra at different pH. Fitted peaks related to Cu(I) (932.4 eV) and Cu(II) (934.6 eV) oxidation states of copper and their corresponding shake-up satellites (938 to 946 eV) are observed. At pH of 9.5, the Cu(I) peak is dominant.[55] As can be seen for samples obtained at a pH of 10.5, a large peak at ~934.6 eV is obtained, corresponding to $Cu2p_{3/2}$ in Cu(II) oxide.[56] The peak intensities of shake-up satellites increase consequently due to the open $3d^9$ shell of Cu(II).[57] In the sample obtained at the pH of 11, the peak related to the Cu(I) oxidation state emerges again. In Fig. 3B, the peak at 531.7 eV is assigned to the ejected electrons from the O 1s of Cu(II) oxide, while a very small peak at ~530.4 eV is also seen, which generally represents the O 1s of Cu(I) oxide. The XPS results of two samples obtained at the pH of 10 and 11 have similar patterns, and an increase is seen for the oxygen O 1s peak at ~530.4 eV relative to that at ~531.7 eV, which indicates the presence of Cu_2O at a much higher concentration in the sample compared to that synthesised at the pH of 10.5. This observation is also confirmed by the dominance of the $Cu2p_{3/2}$ peak at the lower binding energy. This lower binding energy has a much higher intensity for the sample obtained at the pH of 9.5. The XPS observations are in good agrement with the Raman spectroscopy assessments.

To conduct phase quantification on these products, reference samples of cupric and cuprous oxides and their mixtures (1× Cu_2O, 1× CuO, 2× 50 : 50 mixture of Cu_2O : CuO) were prepared. Fig. S1A (ESI†) shows the XRD patterns of these samples. In Fig. S1B (ESI†), Rietveld quantification analysis with automatic mode and semi-automatic mode reflects the actual compositions of the prepared reference samples, which agree with the measured weights of each component before mixing, confirming the validity of this method to quantify copper oxide phases. Phase investigations of the as-synthesised sheets further confirm the phases that were indicated by Raman and XPS analyses (Fig. 4A). These phases and their percentages from Rietveld quantification analysis are presented in Fig. 4B.

The optical band gap of the produced samples was obtained, as shown in Fig. 5A. The sample synthesised at pH = 9.5 shows an absorption edge at 626 nm, which corresponds to the band gap of 1.98 eV. This is close to the direct band gap value of Cu_2O, as has been previously reported.[37]

The emergence of Cu_2O at pH = 9.5 is in agreement with the Raman spectroscopy, XRD and XPS results. Instead, when the pH is 10, 10.5 and 11, absorption edges at approximately ~1055 nm appear (Fig. 5B), which correspond to the band gaps in the regions of 1.16–1.17 eV. This optical bad gap is generally a characteristic absorption edge of CuO.[58,59] Tauc plots can be found in the ESI† (Fig. S2).

The morphology analysis of samples obtained at different pH is presented in Fig. 6. As can be seen, all samples consist of planar bases as the first templated growth onto the liquid metal and then secondary growth emerges from these sheets. It is possible to avoid the secondary growth by limiting the reaction time, so smooth thin sheets (~4 nm thickness) can be obtained (Fig. S3 and S4, ESI†). In Fig. 6, the samples were exfoliated from the surface of the bulk liquid metal for SEM imaging, and thus the printed sheets show large folds. From the SEM images, it is obvious that the largest surface to volume ratio of the

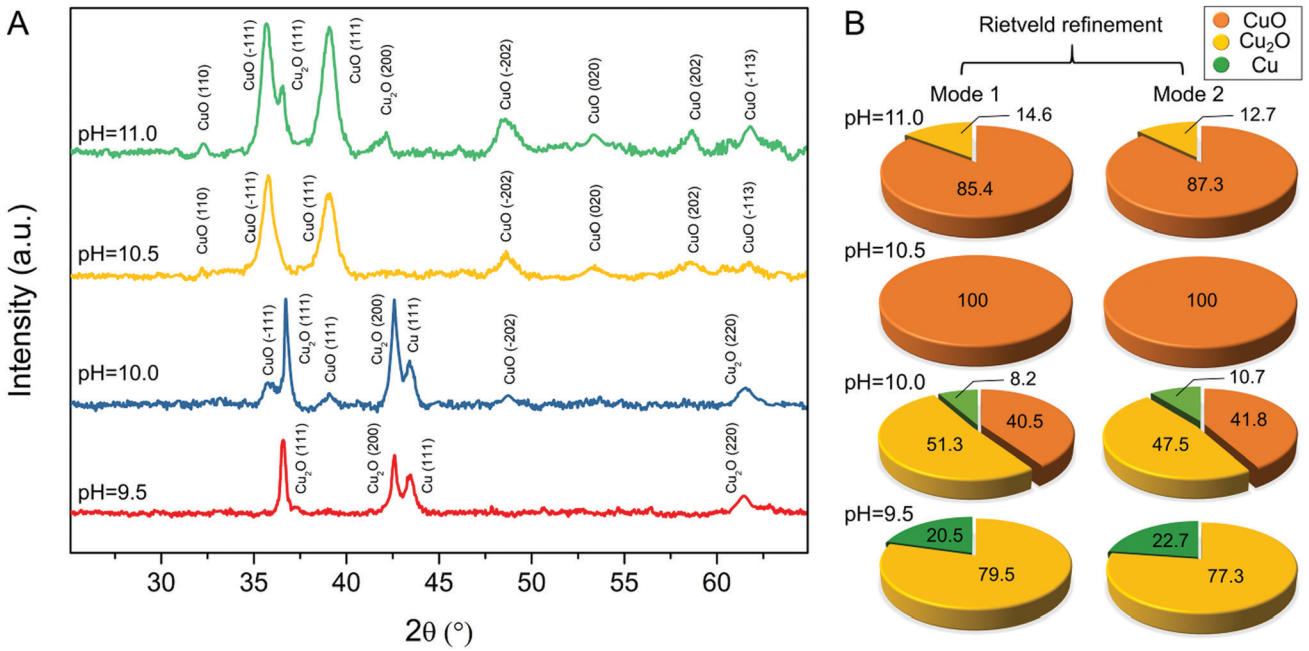

Fig. 4 Phase identification analysis of the Cu_xO products exfoliated from the surface of liquid metal. (A) XRD patterns. (B) Rietveld phase quantification results.

secondary growth is obtained at the pH of 10.5. Considering the highest surface to volume ratio of this sample and its optical band gap, which is that of CuO at 1.16 eV, this sample was chosen for the photodegradation experiments. As such, this sample was further analysed *via* HRTEM.

Concluded from the SEM analysis, Fig. 7A shows a schematic representation of the exfoliated Cu_xO sheets and the secondary dendritic growth of the sample obtained at the pH of 10.5. HRTEM analysis of the secondary growth (Fig. 7B) reveals crystalline structures with sharp tips of the order of several nm radius.

The selected area electron diffraction (SAED) pattern of the edges of the secondary growth displays diffraction rings of (110), (111), (022), (131), (−202), and (−222) of a typical CuO crystal. In Fig. 7C, an interlayer spacing of 2.3 Å, equivalent to the interlayer spacing of (111) in CuO, is observed. In Fig. 7D, the HRTEM analysis shows that the sheets exfoliated from the LM surface are made of wrinkled two-dimensional connected islands. The wrinkled edges have a thickness of approximately 5.3 Å, as highlighted in Fig. 7E. The SAED pattern features diffraction rings derived from the CuO crystal. The high-magnification HRTEM image, shown in Fig. 7F, shows crystallite domains (or lattice fringes) with an interlayer spacing of 2.3 Å, corresponding to the (111) interlayer spacing of the CuO crystal. The high crystallinity is indicated from the inverse fast Fourier transform images (inset of Fig. 7F).

Variations in pH (from 9.5 to 11) induce ion interconversion of copper species within the system. Such pH dependent speciation yields different copper products at the interface. Considering the characterisation results and the past literature, we propose a pathway for the formation of CuO, Cu_2O and Cu.

At the pH of 10.5, it has been suggested that due to the presence of the reactive gallium ions ($HGaO_3^{2-}$) adsorbed with high local concentration at the interface with copper ions $[Cu(OH)_3]^-$, and after hydration, they produce $[Ga(OH)_4]^-$ or $[Ga_{13}O_4(OH)_{24}(H_2O)_{12}]^{7+}$ and hydroxyl ions together with the final product of CuO.[60]

The proposed formation of Cu_2O, which occurs at the pH of 10 and 11, is suggested to take the following pathway:[61]

$$6[Cu(OH)_3]^- + 2Ga \rightarrow 2[Ga(OH)_4]^- + 3Cu_2O + 3H_2O + 4OH^- \quad (1)$$

At the lower pH of 9.5, there is a possibility that direct galvanic replacement can also occur simultaneously together with eqn (1) to produce copper:

$$3[Cu(OH)_3]^- + 2Ga \rightarrow 2[Ga(OH)_4]^- + 3Cu + OH^- \quad (2)$$

To show the functionality of the copper oxide synthesised here, it was grown on smaller liquid metal droplets that could be suspended in solution, and the viability of the suspensions was investigated for photodegradation. Afterwards, the most suitable suspension was tested for photodegradation of a model dye. For the formation of the suspensions of CuO–galinstan droplets, first, the droplets were obtained using a sonication method. Subsequently, the same approach of developing Cu_xO, which was used for creating materials on the surface of large size galinstan droplets, was adopted but with the micronised LM (micro and nano droplets). Heterojunctions of micronised LM–Cu_xO were synthesised. The SEM images in Fig. S5 (ESI†) show the samples obtained at the pH of 9.5, 10, 10.5 and 11. Similar nanostructured Cu_xO morphologies to those of large size droplets were observed in the case of the micronised LM; liquid metal cores covered with sheets of copper oxides with secondary growth originating from these sheets. Samples that were obtained at the pH of 9.5 and 10 were different. They seem to be made of

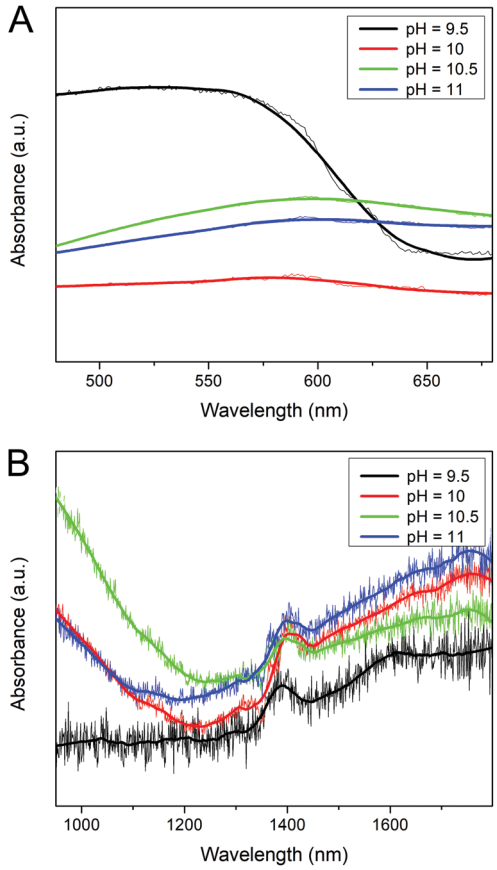

Fig. 5 Light absorption spectra of the Cu_xO products. (A) The visible light absorption in the wavelength range of 480 to 680 nm. (B) The near infrared light absorption in the range of 950 to 1800 nm.

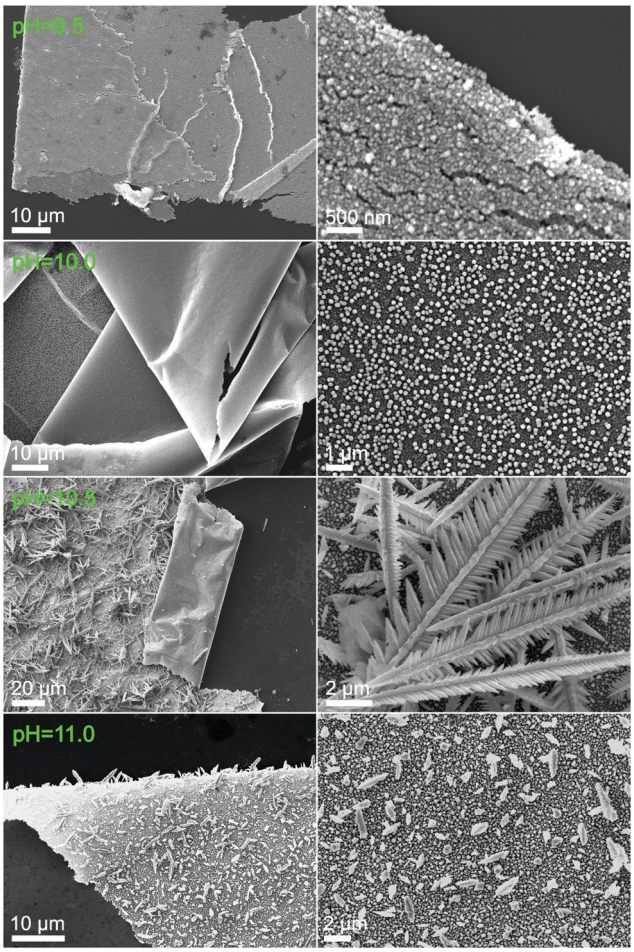

Fig. 6 Morphological analysis of the Cu_xO sheets obtained at different pH. Samples were exfoliated from the bulk liquid metal on the Si wafer.

basal sheets with more compact grains grown on their surface (Fig. S5, ESI†). A sample obtained at the pH of 11 has small traces of dendrimer growth while the majority of the structure is also similar to that of 9.5 and 10 pH samples. In the sample obtained at the pH of 10.5, a combination of expanded dendrite CuO branches on basal sheets is grown on small LM droplets (here referred to as CuO–LM composites). Furthermore, we also investigated the impact of temperature on the formation of nanostructured CuO (Fig. S6, ESI†). We found that heating the reaction system can significantly improve the formation with more dendrite structures observed using SEM. Apart from this, the difference in temperatures (50, 75, 100 and 125 °C) seems to create very little difference among the samples.

As previously shown, the sample produced at the pH of 10.5 consists of CuO with a dominant bandgap of 1.16 eV. This sample was selected for photodegradation experiments since it can show the highest light absorption and interaction with the dye. Methylene blue was chosen as the model molecule as it has been extensively studied for photocatalysis with copper oxides and their composites. The photocatalytic activity of the synthesised CuO–LM composite was assessed under one sunlight intensity for 120 min. Methylene blue has a characteristic peak of 665 nm; with the methylene blue being degraded, the absorbance intensity of the sample decreased, which was determined by measuring its UV-vis spectra at 5, 10, 30, 60, 90, and 120 min. Fig. 8(A) and (B) summarize the photocatalytic performance of the CuO–LM composite. The absorbance intensity of methylene blue dropped substantially for the first 30 min of sunlight irradiation and then further dropped steadily towards a complete degradation at the end of 120 min of experimental time. It can be seen that the CuO–LM composites synthesised in this work could photodegrade the dye to 90% of its initial intensity within ~60 min.

The photocatalytic activity observed for our composite is high compared to the previously reported single phase CuO or other CuO composites (Table S1, ESI†). We deduce that such an extraordinary enhancement came from the synergistic effect between the LM and CuO at the interface. CuO is a p-type material that is placed on the metallic pool of LM. This forms a very strong Schottky type heterojunction that can separate electrons and holes generated by the exposure to the sun simulator inside the CuO semiconductor. The dendrite structure of CuO is another possible reason for the enhancement because its geometry could offer a larger specific surface area than any other reported nanostructures.

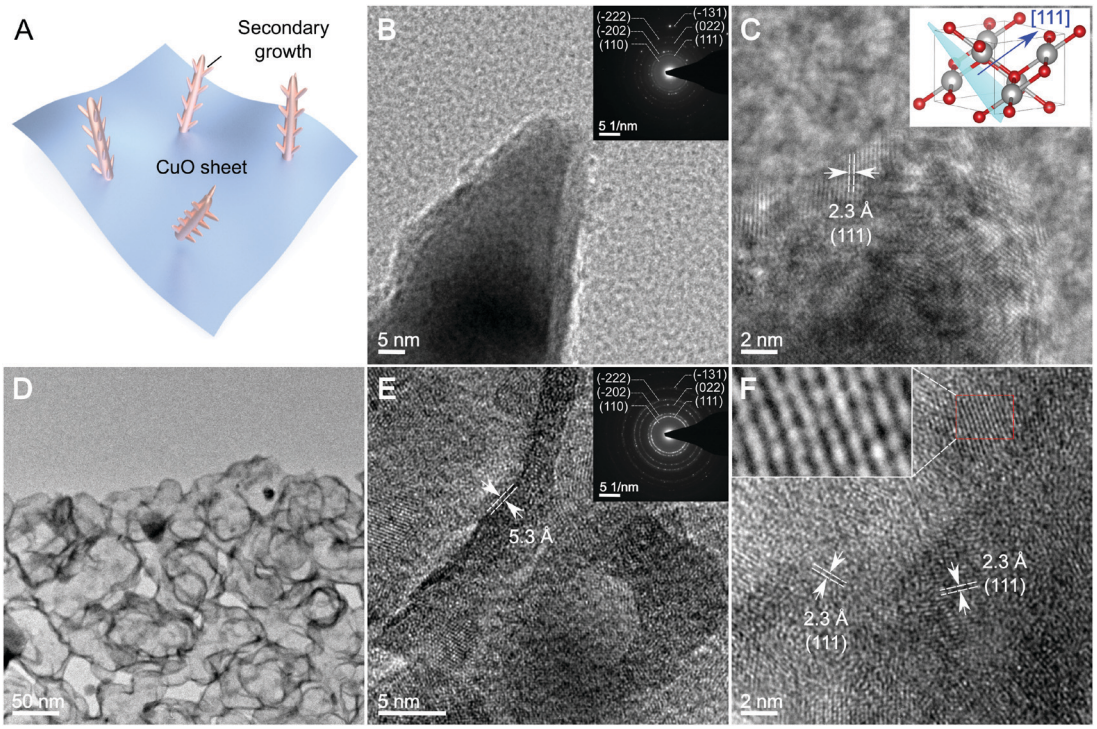

Fig. 7 Morphological and structural analysis of the sheets exfoliated from the bulk LM at the pH of 10.5. (A) A schematic representation of the sheets obtained at the pH of 10.5. (B and C) HRTEM images of the dendritic secondary growth. Inset of (B) shows the SAED patterns. Inset of (C) shows the unit cell of CuO crystal with the (111) crystallographic plane highlighted. (D–F) HRTEM images of basal bases or sheets exfoliated from the bulk LM. Inset of (E) shows the SAED patterns of CuO sheets. Inset of (F) shows the selected area inverse fast Fourier transform images.

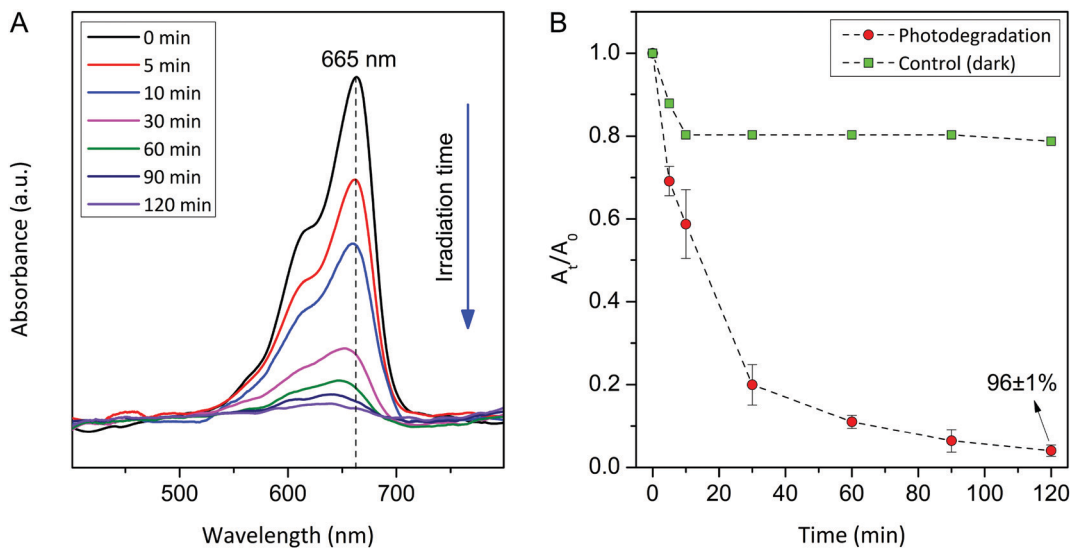

Fig. 8 Photocatalytic activity assessment of CuO–LM composites. (A) UV-vis absorption spectra of methylene blue in the presence of 0.2 mg mL^{-1} CuO–LM composite over time after different durations of solar light irradiation. (B) Time-dependent photodegradation of methylene blue under visible light in the presence of 0.2 mg mL^{-1} CuO–LM composite.

Conclusions

We have demonstrated a practical and controllable room temperature approach of templated synthesis of CuO at the interface of the LM. The ultra-smoothness and distinct chemistry of LM interfaces beget uniform planar structures at the bases and unique morphologies originating from them. The manipulation of interfacial chemistry of the LM gives rise to distinct compositions and morphologies. Here, fixing the pH to 10.5 produced single phase CuO with unique planar and dendritic morphologies on the surface of the LM. Depending on the final application, such an interfacial product can be either exfoliated from the bulk

of the LM or allowed on the LM micro and nano droplets to form semiconductor–metal composites. The optical analysis of the obtained product confirmed the low band gap of the synthesised CuO of 1.16 eV. The HRTEM analysis of the planar morphology revealed ultrathin two-dimensional sheets made of crumbled connected islands of CuO. Further dendritic growth on these sheets was CuO, as confirmed by HRTEM. Such a combination of a low band gap and a large surface area of the metal oxide–LM is ideal for catalytic applications such as photodegradation. As such, a synthesised CuO–LM composite was utilised for testing photodegradation of a model dye, methylene blue. Our composite achieved a superior photocatalytic performance, in comparison to the previous reports, with more than 90% of the dye degraded within ~60 min. Altogether, this work lays the foundation for synthesising metal oxides and their composites with unique nanostructures, considering that this approach can achieve the minimum energy input owing to the unprecedented chemically and catalytically reactive interface that the LM offers. The unprecedented surface of the LM offers extensive possibilities for industrial synthesis and should be thoroughly explored for fabricating functional devices.

Author contributions

H. L. carried out and conceived the experiments, analysed data and wrote the manuscript. R. A. helped with the XRD analysis. Y. W. helped with the synthesis experiments. F. M. A. helped with the photodegradation experiments. S. A. S. helped with the equipment set-up associated with photodegradation and UV. M. A. R. provided useful suggestions. J. Y. helped with UV analysis. M. S. M. and J. T. helped with SEM analysis. R. J., P. K. and M. B. G. discussed the project. K. K. initiated the work, provided intellectual and financial support for the project and participated in writing and polishing the manuscript. M. M. provided direction and guidance, performed experiments, and participated in writing and polishing the manuscript. All authors have reviewed the manuscript and contributed to the intellectual discussions.

Conflicts of interest

There are no conflicts to declare.

Acknowledgements

The authors would like to acknowledge the Australian Research Council (ARC) Laureate Fellowship grant (FL180100053) and the ARC Centre of Excellence FLEET (CE170100039) for the financial support of this work.

References

1 K. Kalantar-Zadeh, J. Tang, T. Daeneke, A. P. O'Mullane, L. A. Stewart, J. Liu, C. Majidi, R. S. Ruoff, P. S. Weiss and M. D. Dickey, *ACS Nano*, 2019, **13**, 7388–7395.
2 A. Zavabeti, J. Z. Ou, B. J. Carey, N. Syed, R. Orrell-Trigg, E. L. Mayes, C. Xu, O. Kavehei, A. P. O'Mullane, R. B. Kaner, K. Kalantar-zadeh and T. Daeneke, *Science*, 2017, **358**, 332–335.
3 L. Sheng, J. Zhang and J. Liu, *Adv. Mater.*, 2014, **26**, 6036–6042.
4 M. Khondoker and D. Sameoto, *Smart Mater. Struct.*, 2016, **25**, 093001.
5 A. Tabatabai, A. Fassler, C. Usiak and C. Majidi, *Langmuir*, 2013, **29**, 6194–6200.
6 A. Fassler and C. Majidi, *Adv. Mater.*, 2015, **27**, 1928–1932.
7 M. D. Bartlett, A. Fassler, N. Kazem, E. J. Markvicka, P. Mandal and C. Majidi, *Adv. Mater.*, 2016, **28**, 3726–3731.
8 M. D. Dickey, R. C. Chiechi, R. J. Larsen, E. A. Weiss, D. A. Weitz and G. M. Whitesides, *Adv. Funct. Mater.*, 2008, **18**, 1097–1104.
9 M. Shafiei, F. Hoshyargar, N. Motta and A. P. O'Mullane, *Mater. Des.*, 2017, **122**, 288–295.
10 L. Hu, L. Wang, Y. Ding, S. Zhan and J. Liu, *Adv. Mater.*, 2016, **28**, 9210–9217.
11 H. Song, T. Kim, S. Kang, H. Jin, K. Lee and H. J. Yoon, *Small*, 2019, 1903391.
12 Y. Yu and E. Miyako, *Angew. Chem.*, 2017, **129**, 13794–13799.
13 S. A. Chechetka, Y. Yu, X. Zhen, M. Pramanik, K. Pu and E. Miyako, *Nat. Commun.*, 2017, **8**, 15432.
14 Y. Yu and E. Miyako, *iScience*, 2018, **3**, 134–148.
15 M. B. Ghasemian, M. Mayyas, S. A. Idrus-Saidi, M. A. Jamal, J. Yang, S. S. Mofarah, E. Adabifiroozjaei, J. Tang, N. Syed, A. P. O'Mullane and K. Kalantar-Zadeh, *Adv. Funct. Mater.*, 2019, **29**, 1901649.
16 H. J. Um, G. D. Kong and H. J. Yoon, *ACS Appl. Mater. Interfaces*, 2018, **10**, 34758–34764.
17 T. Daeneke, K. Khoshmanesh, N. Mahmood, I. De Castro, D. Esrafilzadeh, S. Barrow, M. Dickey and K. Kalantar-Zadeh, *Chem. Soc. Rev.*, 2018, **47**, 4073–4111.
18 W. Zhang, B. S. Naidu, J. Z. Ou, A. P. O'Mullane, A. F. Chrimes, B. J. Carey, Y. Wang, S.-Y. Tang, V. Sivan, A. Mitchell, S. K. Bhargava and K. Kalantar-Zadeh, *ACS Appl. Mater. Interfaces*, 2015, **7**, 1943–1948.
19 W. Zhang, J. Z. Ou, S. Y. Tang, V. Sivan, D. D. Yao, K. Latham, K. Khoshmanesh, A. Mitchell, A. P. O'Mullane and K. Kalantar-zadeh, *Adv. Funct. Mater.*, 2014, **24**, 3799–3807.
20 J. Yan, Y. Lu, G. Chen, M. Yang and Z. Gu, *Chem. Soc. Rev.*, 2018, **47**, 2518–2533.
21 M. G. Mohammed and R. Kramer, *Adv. Mater.*, 2017, **29**, 1604965.
22 Q. Wang, Y. Yu, J. Yang and J. Liu, *Adv. Mater.*, 2015, **27**, 7109–7116.
23 M. M. Alsaif, S. Kuriakose, S. Walia, N. Syed, A. Jannat, B. Y. Zhang, F. Haque, M. Mohiuddin, T. Alkathiri, N. P. Pilla, T. Daeneke, J. Z. Ou and A. Zavabeti, *Adv. Mater. Interfaces*, 2019, **6**, 1900007.
24 M. D. Dickey, *Adv. Mater.*, 2017, **29**, 1606425.
25 Y. Gao, H. Li and J. Liu, *PLoS One*, 2012, **7**, e45485.
26 S. A. Idrus-Saidi, J. Tang, M. B. Ghasemian, J. Yang, J. Han, N. Syed, T. Daeneke, R. Abbasi, P. Koshy, A. P. O'Mullane

and K. Kalantar-Zadeh, *J. Mater. Chem. A*, 2019, **7**, 17876–17887.
27 J. Tang, R. Daiyan, M. B. Ghasemian, S. A. Idrus-Saidi, A. Zavabeti, T. Daeneke, J. Yang, P. Koshy, S. Cheong, R. D. Tilley, R. B. Kaner, R. Amal and K. Kalantar-Zadeh, *Nat. Commun.*, 2019, **10**, 4645.
28 F. Hoshyargar, J. Crawford and A. P. O'Mullane, *J. Am. Chem. Soc.*, 2017, **139**, 1464–1471.
29 N. Taccardi, M. Grabau, J. Debuschewitz, M. Distaso, M. Brandl, R. Hock, F. Maier, C. Papp, J. Erhard and C. Neiss, *Nat. Chem.*, 2017, **9**, 862–867.
30 M. R. Khan, C. B. Eaker, E. F. Bowden and M. D. Dickey, *Proc. Natl. Acad. Sci. U. S. A.*, 2014, **111**, 14047–14051.
31 F. Centurion, M. G. Saborío, F. M. Allioux, S. Cai, M. B. Ghasemian, K. Kalantar-Zadeh and M. A. Rahim, *Chem. Commun.*, 2019, **55**, 11291–11294.
32 N. Syed, A. Zavabeti, J. Z. Ou, M. Mohiuddin, N. Pillai, B. J. Carey, B. Y. Zhang, R. S. Datta, A. Jannat, F. Haque, K. A. Messalea, C. Xu, S. P. Russo, C. F. McConville, T. Daeneke and K. Kalantar-Zadeh, *Nat. Commun.*, 2018, **9**, 3618.
33 S. Mosleh, M. R. Rahimi, M. Ghaedi, K. Dashtian and S. Hajati, *Ultrason. Sonochem.*, 2018, **40**, 601–610.
34 C. Dong, M. Zhong, T. Huang, M. Ma, D. Wortmann, M. Brajdic and I. Kelbassa, *ACS Appl. Mater. Interfaces*, 2011, **3**, 4332–4338.
35 A. S. Zoolfakar, M. Z. Ahmad, R. A. Rani, J. Z. Ou, S. Balendhran, S. Zhuiykov, K. Latham, W. Wlodarski and K. Kalantar-Zadeh, *Sens. Actuators, B*, 2013, **185**, 620–627.
36 N. Zayyoun, L. Bahmad, L. Laânab and B. Jaber, *Appl. Phys. A: Mater. Sci. Process.*, 2016, **122**, 488.
37 A. S. Zoolfakar, R. A. Rani, A. J. Morfa, A. P. O'Mullane and K. Kalantar-Zadeh, *J. Mater. Chem. C*, 2014, **2**, 5247–5270.
38 S. M. Pawar, J. Kim, A. I. Inamdar, H. Woo, Y. Jo, B. S. Pawar, S. Cho, H. Kim and H. Im, *Sci. Rep.*, 2016, **6**, 21310.
39 Y. Lu, X. Liu, K. Qiu, J. Cheng, W. Wang, H. Yan, C. Tang, J.-K. Kim and Y. Luo, *ACS Appl. Mater. Interfaces*, 2015, **7**, 9682–9690.
40 V. Scuderi, G. Amiard, S. Boninelli, S. Scalese, M. Miritello, P. Sberna, G. Impellizzeri and V. Privitera, *Mater. Sci. Semicond. Process.*, 2016, **42**, 89–93.
41 Y. Zhao, C. Wang and G. G. Wallace, *J. Mater. Chem. A*, 2016, **4**, 10710–10718.
42 A. M. Mansour, E. M. El Bakry and N. T. Abdel-Ghani, *J. Photochem. Photobiol., A*, 2016, **327**, 21–24.
43 M. Kumar, R. R. Das, M. Samal and K. Yun, *Mater. Chem. Phys.*, 2018, **218**, 272–278.
44 A. Tadjarodi, O. Akhavan and K. Bijanzad, *Trans. Nonferrous Met. Soc. China*, 2015, **25**, 3634–3642.
45 A. Raizada, D. Ganguly, M. M. Mankad, R. Krishna and B. Nagabhushana, *Chem. Eng. Res.*, 2014, **2**, 249–258.
46 M. Yang and J. He, *J. Colloid Interface Sci.*, 2011, **355**, 15–22.
47 R. Saravanan, S. Karthikeyan, V. Gupta, G. Sekaran, V. Narayanan and A. Stephen, *Mater. Sci. Eng., C*, 2013, **33**, 91–98.
48 L. Zhu, M. Hong and G. W. Ho, *Nano Energy*, 2015, **11**, 28–37.
49 L. Sun, G. Wang, R. Hao, D. Han and S. Cao, *Appl. Surf. Sci.*, 2015, **358**, 91–99.
50 S. Meshram, P. Adhyapak, U. Mulik and D. Amalnerkar, *Chem. Eng. J.*, 2012, **204**, 158–168.
51 Y. Wang, D. Wang, B. Yan, Y. Chen and C. Song, *J. Mater. Sci.: Mater. Electron.*, 2016, **27**, 6918–6924.
52 D. Powell, A. Compaan, J. Macdonald and R. Forman, *Phys. Rev. B: Solid State*, 1975, **12**, 20–25.
53 J. Xu, W. Ji, Z. Shen, W. Li, S. Tang, X. Ye, D. Jia and X. Xin, *J. Raman Spectrosc.*, 1999, **30**, 413–415.
54 S. Kabuyanagi, T. Nishimura, T. Yajima and A. Toriumi, *AIP Adv.*, 2016, **6**, 015114.
55 W. Zhang, B. Wang, C. Hao, Y. Liang, H. Shi, L. Ao and W. Wang, *J. Alloys Compd.*, 2016, **684**, 445–452.
56 F. Klein, R. Pinedo, P. Hering, A. Polity, J. r. Janek and P. Adelhelm, *J. Phys. Chem. C*, 2016, **120**, 1400–1414.
57 M. Swadźba-Kwaśny, L. Chancelier, S. Ng, H. G. Manyar, C. Hardacre and P. Nockemann, *Dalton Trans.*, 2012, **41**, 219–227.
58 D. Gupta, S. Meher, N. Illyaskutty and Z. C. Alex, *J. Alloys Compd.*, 2018, **743**, 737–745.
59 Y. Yang, D. Xu, Q. Wu and P. Diao, *Sci. Rep.*, 2016, **6**, 35158.
60 L. A. Wills, X. Qu, I. Y. Chang, T. J. Mustard, D. A. Keszler, K. A. Persson and P. H. Y. Cheong, *Nat. Commun.*, 2017, **8**, 15852.
61 R. C. Ropp, *Encyclopedia of the alkaline earth compounds*, Newnes, 2012.